Optical study of the anisotropic erbium spin flip-flop dynamics

B. Car,[1] L. Veissier,[1] A. Louchet-Chauvet,[1] J.-L. Le Gouët,[1] and T. Chanelière[1,2]

[1]*Laboratoire Aimé Cotton, CNRS, Université Paris-Sud, ENS-Cachan, Université Paris-Saclay, 91405 Orsay, France*
[2]*Université Grenoble Alpes, CNRS, Grenoble INP, Institut Néel, 38000 Grenoble, France*

We investigate the erbium flip-flop dynamics as a limiting factor of the electron-spin lifetime and more generally as an indirect source of decoherence in rare-earth-doped insulators. Despite the random isotropic arrangement of dopants in the host crystal, the dipolar interaction strongly depends on the magnetic field orientation following the strong anisotropy of the g factor. In $Er^{3+} : Y_2SiO_5$, we observe in a 10-ppm doped sample a 3 orders-of-magnitude variation of the erbium flip-flop rate, as expected from the dipolar coupling term between identical spins with an anisotropic g tensor. We can estimate the correct order of magnitude for a 50-ppm concentration, but we can only reproduce qualitatively the orientational variation of the flip-flop rate.

I. INTRODUCTION

Rare-earth ions are appealing qubits to store and process quantum information. When embedded in crystalline matrices, they combine well-protected spin and optically active transitions. The interplay between the spin and atomiclike optical excitations places the rare-earth species at the interface between solid-state and atomic physics. Within the lanthanide series, the Kramers ions (odd number of electrons) exhibit a strong paramagnetic sensitivity because of the crystal field levels admixture, leading to a large anisotropic effective electron spin [1]. They also hold a lot of promises in quantum information, because a moderate bias magnetic field induces electron paramagnetic resonances (EPR) in the few-gigahertz range. This typical splitting falls in the range of superconducting qubits to form a hybrid interface between the actively investigated quantum electronics circuits and solid-state spins as a memory buffer [2,3]. Additionally, the noticeably narrow inhomogeneous line ($\sim$1 GHz) is well resolved at low field, thus allowing the spectral optical addressing of spin-selective transitions. The convergence of the appealing spin and optical properties has recently attracted a lot of attention to promote Kramers paramagnetic ions as a quantum spin-photon interface with highly diluted samples [4–6] or more recently, with single ions [7,8]. Among them, erbium is emblematic because its optical transition falls in the telecom range and it exhibits large g-factor values ($g \sim 15$) in some crystals such as $Er^{3+} : Y_2SiO_5$ or $Er^{3+} : LiNbO_3$ [9–11]. The tribute to pay to these attractive properties is a rapid loss of decoherence due to the enhanced sensitivity to the magnetic fluctuations. Whatever the viewing angle, optics or EPR, the spin dynamical properties are absolutely critical. They obviously directly impact the outcome of the EPR spectroscopy, but they also influence the optical coherence time by the differential magnetic fluctuations between the ground and optically excited states [12].

The spin dynamics is essentially governed by two mechanisms [12]. On the one side, spin lattice relaxations (SLR) describe the interaction of the spin with the phonon bath [13]. They can be detailed in different mechanisms, namely, direct, Raman, and Orbach, depending on the process order (one- or two-phonon) and the level diagram (on- or off-resonance phonon interaction). However, at liquid helium temperatures, the two-phonon processes are usually negligible. Thus, the SLR is dominated by the direct process. On the other side, the cross-relaxation between adjacent impurities with opposite spin orientations, also known as the flip-flop mechanism (FF), appears as an important process even in low-doping samples [14,15]. Both SLR an FF mechanisms primarily describing the population decay, or in other words, the longitudinal relaxation, indirectly induce decoherence. Indeed, the fluctuations of the spins generate a background noise leading to decoherence, or transverse relaxation. SLR and FF have very different dependencies as a function of the applied magnetic field [12,16,17]. Practically, SLR dominates at large field and FF at low field. As the magnetic field energy splitting increases and becomes larger than k_BT (where k_B is the Boltzmann constant and T the temperature), the spins become fully polarized, thus preventing the FF. At the same time, the phonon density increases, making the SLR more efficient. At the end, SLR and FF are well separated and can be considered and fought independently to prevent relaxation. At large magnetic fields, SLR can be controlled by adjusting the level structure with respect to the photon density. This can be done, for example, by a clever orientation of the magnetic field relying on the highly anisotropic Zeeman interaction [18,19] or by a direct nanostructuration of the material to control the intrinsic phonon density [20–22]. FF can be also avoided by cooling the spins to a few tens of mK, thus benefiting from a fully polarized sample at thermal equilibrium. By going deep into the SLR regime, the phonon-bottleneck relaxation has been observed very recently at 20 mK [23].

The low-field limit at larger temperature, typically in the 2–4 K range, also deserves consideration because it offers relaxed experimental conditions. As previously mentioned, with a few gigahertz Zeeman splitting and well-resolved optical transitions, this is a region of interest for quantum information applications. The FF dominates the spin dynamics in that

case. A partial optical spin polarization can be obtained by frequency-selective optical pumping, also known as spectral hole burning [16,17,24]. The imprinted spectral pattern, usually burned during the preparation stage of quantum memory protocols [25], and references therein], has a lifetime limited by the FF mechanism. The reader more familiar with EPR measurements may be confused by the translation of the FF mechanism into a population decay. The optical technique, spectral hole burning, selects a small fraction of the spins (less than 1% for a typical hole linewidth as compared to the inhomogeneous broadening). The flip-flop mechanism mostly involves an optically probed spin which is cross-relaxing with an unprobed spin. This translates into a population decay for the probed ensemble. Motivated by the potential applications and more generally by the possibility to optically control the out-of-equilibrium ensemble polarization, we optically study the FF cross-relaxation process between erbium spins.

As previously discussed in the case of Nd^{3+} : Y_2SiO_5, an order-of-magnitude anisotropy in the *g* factor should translate into 4 orders of magnitude for the FF rate [17], Supplemental Material]. As pointed out by Cruzeiro *et al.*, the predicted angular variation of the FF rate still needs to be confirmed experimentally [17], Supplemental Material]. This is the focus of the present paper. We intentionally apply low magnetic fields where the dynamics is dominated by the FF relaxation. At low field (a few mT), the SLR mechanism can indeed be fully discarded. As a rough estimation, one can, for example, notice that the SLR rate leads to a 10–100 ms relaxation time for a magnetic field B $\sim$ 0.1–1 T for a Kramers doublet [12,17]. The SLR rate scales as B^4, so a reduction of the magnetic field by an order of magnitude leads to a SLR relaxation time in the range of tens or hundreds of seconds at minimum. This is in any case much longer than the FF lifetimes that will be considered in the following.

The strong angular variation that we study here may have a serious impact if the crystal is not properly oriented. In others words, when the low-magnetic-field dynamics is considered, any evaluation of the cross-relaxation between Kramers ions based on an average effective isotropic *g* factor should be handled with extreme precautions.

The paper is organized as follows. We first focus on the dipolar coupling between two identical spins with fully anisotropic *g* tensors and explain how this mechanism leads to an expected anisotropic FF rate (Sec. II). This description can be seen as the extension and the generalization of previous work [17], Supplemental Material]. We then use optical techniques (transient excitation and accumulated spectral hole burning) to measure the anisotropy of the FF rate of Er^{3+} in Y_2SiO_5 as a function of the magnetic field orientation for two concentrations of 10 and 50 ppm (Sec. III). We verify that the lifetime varies by several orders of magnitude, as expected from the *g*-tensor theoretical calculation. The experimental results are finally analyzed and discussed in light of an elementary model whose fitting variables can serve as an estimate of microscopic parameters (Sec. IV).

II. DIPOLAR COUPLING ANISOTROPY IN THE CASE OF Er^{3+} : Y_2SiO_5

We here discuss the origins of the flip-flop anisotropy by considering the dipole-dipole interaction between identical

spins. This dynamics has been investigated in the context of spin diffusion in a broad sense (spatial and spectral) [26], chap. 4, Spin diffusion in solids]. Starting from the seminal work of Bloembergen *et al.* [27,28], this is still an active subject of research widely stimulated by the perspectives in quantum information for which spin impurities in solids appear as a useful resource [29], and references].

The conventional perturbative approaches are based on Fermi's golden rule (FGR). Despite a historical prevalence [27,28] and a good ability to rapidly extract orders of magnitude [30], Mims, Chap. 4, p. 294], the approaches based on the FGR appear limited to fully predict the spin ensemble dynamics. The most sophisticated models account for the different dipole-dipole pairs in the crystal and subsequently average the obtained decay curves [31]. This leads to nonexponential decays that would be challenging to distinguish in our case from a multiexponential curve that we observe because of the different decay channels and ion species (see Sec. IV). The so-called stretched exponential can be obtained in the limit of a continuous spatial distribution of impurities, but the exact arrangement of the spins and the local range of validity of the perturbative assumption should be handled with precaution [32]. An advanced modeling is not the goal of the present paper, which focuses on the experimental evidence of the anisotropy. Nevertheless, we hope a theoretical effort will be made in this direction.

In order to exploit our experimental results and at minimum extract orders of magnitude for a microscopic description, we will stick to the conventional approach based on the FGR, assume a continuous spatial distribution, and finally, include fitting parameters for the experimental data of Sec. III B.

We start by evaluating the dipolar coupling term between identical spins involved in a flip-flop process. This latter reads as $\langle +-|\mathbf{H}_{ij}|-+\rangle$, where $\mathbf{H}_{ij}$ stands for the magnetic dipole-dipole Hamiltonian of a given i, j ion pair. $|+\rangle$ and $|-\rangle$ are the eigenstates of the Zeeman Hamiltonian. The coupling Hamiltonian explicitly reads as

$$\mathbf{H}_{ij} = -\frac{\mu_0}{4\pi}\frac{1}{r_{ij}^3}[3(\boldsymbol{\mu}_i \cdot \boldsymbol{u}_{ij})(\boldsymbol{\mu}_j \cdot \boldsymbol{u}_{ij}) - \boldsymbol{\mu}_i \cdot \boldsymbol{\mu}_j], \quad (1)$$

where $\boldsymbol{r}_{ij}$, $\boldsymbol{u}_{ij}$, and $\boldsymbol{\mu}_{i,j}$ respectively represent the inter-ion vector, the unit vector along $\boldsymbol{r}_{ij}$, and the magnetic dipole moments.

The term $\langle +-|\mathbf{H}_{ij}|-+\rangle$ drives the flip-flop process. It contains the anisotropy derived from the $\bar{\bar{g}}$-tensor values. More precisely, the magnetic dipole moment $\boldsymbol{\mu}_i$ can indeed be written in terms of the effective spin operator $\hat{\mathbf{S}}_i$ as

$$\boldsymbol{\mu}_i = \mu_B \bar{\bar{g}} \cdot \hat{\mathbf{S}}_i. \quad (2)$$

In the frame (x, y, z) where the $\bar{\bar{g}}$ tensor is diagonal, $\boldsymbol{\mu}_i$ reads as

$$\boldsymbol{\mu}_i = \mu_B(\hat{S}_{i,x}g_x\boldsymbol{u}_x + \hat{S}_{i,y}g_y\boldsymbol{u}_y + \hat{S}_{i,z}g_z\boldsymbol{u}_z), \quad (3)$$

where

$$\bar{\bar{g}} = \begin{pmatrix} g_x & 0 & 0 \\ 0 & g_y & 0 \\ 0 & 0 & g_z \end{pmatrix} \quad (4)$$

and $(\boldsymbol{u}_x, \boldsymbol{u}_y, \boldsymbol{u}_z)$ represent the unit vectors of the reference frame. When $\boldsymbol{B}$ is directed along Oz, $\hat{S}_z$ and the Zeeman Hamiltonian share the same eigenvectors. Hence, $\langle +|\hat{S}_{i,z}|-\rangle$ vanishes and $\langle +-|\mathbf{H}_{ij}|-+\rangle$ does not depend on g_z. Conversely, $\langle +-|\mathbf{H}_{ij}|-+\rangle$ does not depend on g_x or g_y when $\boldsymbol{B}$ is directed along Ox or Oy, respectively. That feature is critical to understand the anisotropy of the coupling mechanism and will prove to be important in the following.

The application of the FGR requires a description of the final states as a continuum of energy states. In that case, for a given target ion i, we choose to represent the different interacting ions j which can induce a FF process as different final states. The coupling term, more precisely, the square of the matrix element, should be replaced by an average value $\langle |\langle +-|\mathbf{H}_{ij}|-+\rangle|^2 \rangle_{Av}$, where $\langle ... \rangle_{Av}$ represents the averaging between the distributed pairs in the crystal.

The FF rate R_{FF} is then evaluated as

$$R_{\text{FF}} = \frac{2\pi}{\hbar}\langle |\langle +-|\mathbf{H}_{ij}|-+\rangle|^2 \rangle_{Av} \times \frac{1}{\hbar\Gamma_g}, \quad (5)$$

where $1/\hbar\Gamma_g$ is the density of final states described by Γ_g representing the spin transition width, or more precisely, its inhomogeneous broadening (in s^{-1}). This is an experimental parameter that can be measured independently, as will be discussed in Sec. IV.

The evaluation of the distribution averaging $\langle ... \rangle_{Av}$ can be taken in the continuous limit. The pairs are randomly distributed with an average distance much larger than the nearest-neighbor separation in the unit cell. Even if the ions seat at a discrete location in the crystal structure, at large distances, the pair distribution appears as continuous [32]. Additionally, the $\mathbf{H}_{ij}$ structure Eq. (1) suggests that the averaging in Eq. (5) can be approximately evaluated as a combination of first angular averaging over the $\boldsymbol{u}_{ij}$ direction and then as a sum over the inter-ion distance $\boldsymbol{r}_{ij}$. Therefore,

$$\langle |\langle +-|\mathbf{H}_{ij}|-+\rangle|^2 \rangle_{Av} \approx \left(\frac{\mu_0}{4\pi}\mu_B^2\right)^2 \times \Xi(\bar{\bar{g}}, \boldsymbol{B}) \times \left\langle \frac{1}{r_{ij}^6}\right\rangle_{Av}, \quad (6)$$

where μ_B denotes the Bohr magneton, and the dimensionless coupling factor $\Xi(\bar{\bar{g}}, \boldsymbol{B})$, resulting from the angular averaging, is defined as a continuous integral:

$$\Xi(\bar{\bar{g}}, \boldsymbol{B}) = \frac{1}{4\pi} \times \mu_B^{-4} \times \int d\boldsymbol{u}_{ij} |\langle +-|3(\boldsymbol{\mu}_i \cdot \boldsymbol{u}_{ij})(\boldsymbol{\mu}_j \cdot \boldsymbol{u}_{ij}) - \boldsymbol{\mu}_i \cdot \boldsymbol{\mu}_j|-+\rangle|^2. \quad (7)$$

This average value depends on the $\bar{\bar{g}}$ tensor and on the $\boldsymbol{B}$ direction, which determines the eigenvectors $(|+\rangle, |-\rangle)$. The detailed calculation of $\Xi(\bar{\bar{g}}, \boldsymbol{B})$ is deferred to Appendix. This first term is responsible for the FF anisotropy and should be analyzed in detail.

The second term $\langle \frac{1}{r_{ij}^6} \rangle_{Av}$ actually raises many questions that will be discussed at the end of this section, Sec. IV. At this level we leave this aside because this term does not depend on the magnetic field orientation, so we focus on $\Xi(\bar{\bar{g}}, \boldsymbol{B})$.

In order to evaluate the dipole-dipole coupling term in $Er^{3+}:Y_2SiO_5$, we consider only the zero-nuclear-spin isotopes (78% of the doping ions), ignoring the ^{167}Er isotope

(22% abundance with nonzero nuclear spin). The FF dynamics of the ^{167}Er is clearly more complex because of the hyperfine structure, as will be discussed in IV. It should be noted that the ^{167}Er population is redistributed between many hyperfine states, which reduces their optical signature as compared to the dominant zero-nuclear-spin isotopes. In any case, the required smallness of the spin-spin interaction with respect to Zeeman splitting (perturbative approach) is satisfied at external magnetic field values as small as 1 mT. In a 10-ppm $Er^{3+}:Y_2SiO_5$ crystal, at $B = 1$ mT, the Zeeman interaction varies between 5 and 50 MHz, depending on the crystal orientation, whereas the Er-Er interaction ranges within 1 and 100 kHz. As we will discuss in Sec. IV, we use a very weak magnetic field to minimize the observed inhomogeneous spin broadening. We choose to keep it constant to $B = 0.3$ mT for experiments on the 10-ppm sample (0.15 mT for the 50 ppm) and vary the field orientation to reveal the anisotropy. The example of $Er^{3+}:Y_2SiO_5$ is particularly interesting because it shows strong anisotropic properties. Indeed, in the frame (x, y, z) where the $\bar{\bar{g}}$ tensor is diagonal,

$$g_z \approx 10\, g_y \approx 30\, g_x. \quad (8)$$

As pointed out above, $\langle +-|\mathbf{H}_{ij}|-+\rangle$ and consequently, $\Xi(\bar{\bar{g}}, \boldsymbol{B})$, depend only on the g_x and g_y components, much smaller than g_z in $Er^{3+}:Y_2SiO_5$, when the applied magnetic field is directed along Oz. According to the general expression derived in Appendix,

$$\Xi(\bar{\bar{g}}, \boldsymbol{B}) = \frac{1}{20}\left(g_x^4 + g_y^4 - g_x^2 g_y^2\right). \quad (9)$$

This situation is almost reached when $\boldsymbol{B}$ is directed at about $\phi = 135°$ from D_1 in the $D_1 - D_2$ plane, or in other words, the principal axis lies almost in the $D_1 - D_2$ plane.

The g_z contribution raises as the $\boldsymbol{B}$ direction departs from Oz, reaching a maximum when $\boldsymbol{B}$ lies in the xOy plane. Then $\Xi(\bar{\bar{g}}, \boldsymbol{B})$ reads as

$$\Xi(\bar{\bar{g}}, \boldsymbol{B}) = \frac{1}{20}\left(g_z^4 + g_\perp^4 - g_z^2 g_\perp^2\right), \quad (10)$$

where

$$\frac{1}{g_\perp^2} = \frac{1}{B^2}\left(\frac{B_x^2}{g_y^2} + \frac{B_y^2}{g_x^2}\right). \quad (11)$$

This situation occurs for $\phi \approx 30°$. According to Eqs. (9) and (10), the FF relaxation rate should scale by a factor of $(g_z/g_y)^4 \simeq 10^4$ between those two situations (neglecting the small g_x contribution). Note that in a scenario where the g tensor is isotropic, $\Xi(\bar{\bar{g}}, \boldsymbol{B})$ would be totally independent of the external magnetic field direction.

We calculate the $\Xi(\bar{\bar{g}}, \boldsymbol{B})$ variation with the external magnetic field $\boldsymbol{B}$ direction in the crystalline frame (D_1, D_2, b). Figure 1 shows the map of $\Xi(\bar{\bar{g}}, \boldsymbol{B})$ following the general expression Eq. (A9) as a function of ϕ and θ the angles of $\boldsymbol{B}$ in the (D_1, D_2, b) frame. We expect strong variations within several planes, including the D_1-D_2 plane that we considered above.

We now come back to the evaluation of the second term $\langle \frac{1}{r_{ij}^6} \rangle_{Av}$. Without any specific assumption on the spin arrangement in the crystal cell, a continuous spatial distribution of impurities can be assumed. In that case, the continuous integral replacing $\langle \frac{1}{r_{ij}^6} \rangle_{Av}$ diverges close to $r_{ij} \to 0$. A minimum
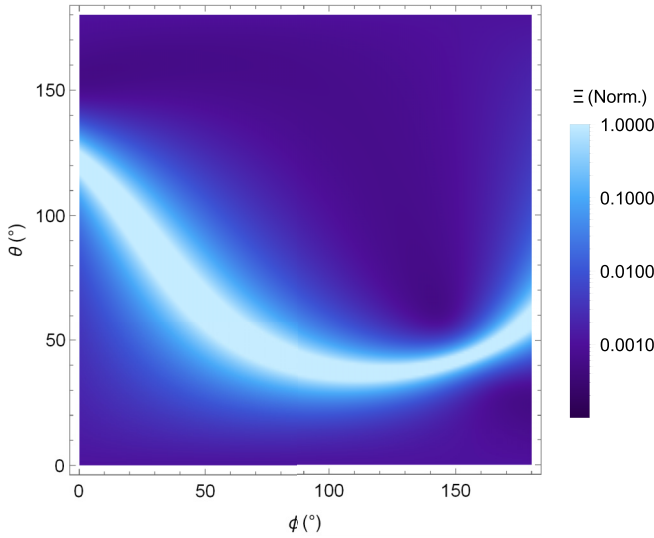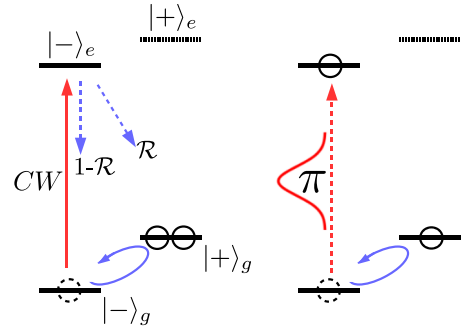
FIG. 2. Optical measurement techniques. (Left) Accumulated spectral hole burning: the spin polarization is obtained by pumping through the optically excited state. (Right) Optical inversion recovery: a spin population imbalance can also be created by transient optical excitation (π pulse typically) when the spin lifetime is much shorter than the optical decay time. See text for details.

FIG. 1. Map of $\Xi(\bar{\bar{g}}, \boldsymbol{B})$ as a function of the orientation of the external magnetic field. The angles ϕ and θ are the angles of the external magnetic field $\boldsymbol{B}$ in the crystalline frame (D_1, D_2, b). When $\theta = 90°$, the field lies in the $D_1 - D_2$ plane. Note the logarithmic color map.

cut-off distance R_0 has to be introduced as in Ref. [32], so we approximate

$$\left\langle \frac{1}{r_{ij}^6} \right\rangle_{Av} \approx \frac{4\pi}{3} \frac{n_s}{R_0^3}. \tag{12}$$

The physical meaning of the R_0 cutoff should be discussed. One could, for example, choose the nearest-neighbor distance between spins. This choice would intrinsically assume that the FGR is valid at any distance between dopants, especially at close distances where the density of final states [given by $1/\hbar\Gamma_g$ in Eq. (5)] may be difficult to define properly. This cut-off distance could alternatively represent the range at which the pairwise interaction is not simply given by the dipole-dipole coupling but may also contain an exchange term [33] or an additional distortion of the crystalline cell because of the dopant ion's proximity, for example. At this elementary level of modeling, we decide to keep R_0 as a free fitting parameter representing the spatial range of validity of Eq. (5) and potentially including different unidentified contributions. We simply scale R_0 by comparison with the average spin distance $1/\sqrt[3]{n_s}$ and introduce a dimensionless parameter α_0 such as $\alpha_0 = n_s R_0^3$:

$$R_{\mathrm{FF}} = \frac{1}{12\hbar^2} \mu_0^2 \mu_{\mathrm{B}}^4 \times \Xi(\bar{\bar{g}}, \boldsymbol{B}) \times n_s^2 \times \frac{1}{\alpha_0 \Gamma_g}. \tag{13}$$

We will leave $\alpha_0 \Gamma_g$ as a free scaling fitting parameter for the two experimental sets of Sec. III B.

III. FLIP-FLOP RATE MEASUREMENTS IN ERBIUM-DOPED Y$_2$SiO$_5$

Because of the strong variation of the expected lifetime, different techniques must be used to cover the measurement range, namely, the accumulated spectral hole burning and the optical inversion recovery. In short, the first technique

is well adapted for the measurement of long spin lifetimes (as compared to the optical lifetime) and the second one for short lifetimes. In practice, when no long-lived spectral hole burning feature is observed, short spin lifetime can be revealed by optical inversion recovery. We first discuss the methodology (relevant level structure and techniques) and then detail the experimental results.

A. Spin lifetime optical measurement techniques

The method of choice to measure optically the spin lifetime is spectral hole burning (SHB) [17,24,34–38]. In a simplified picture, SHB operates as optical pumping in an equivalent three-level system, as represented in Fig. 2 (left). This ideal scheme corresponds well to the case of $Er^{3+} : Y_2SiO_5$. The $^4I_{15/2} \rightarrow {}^4I_{13/2}$ optical transition of Er^{3+} splits into ground and excited Kramers doublets, leading to a four-level structure. The laser frequency determines the spin levels that are addressed by the optical excitation ($|-\rangle_g \rightarrow |-\rangle_e$). We can reduce the structure to a three level by just neglecting $|+\rangle_e$. This simplification is made possible because the direct spin relaxation in the excited state $|-\rangle_e \leftrightarrow |+\rangle_e$ can be neglected. More precisely, in the FF regime, the optically excited spin density is so weak that the $|-\rangle_e \leftrightarrow |+\rangle_e$ cross-relaxation is extremely unlikely [39,40]. The SHB structure consists of three levels, namely, $|-\rangle_g$, $|-\rangle_e$, and $|+\rangle_g$. Instead, if the laser excites the crossed transition $|-\rangle_g \rightarrow |+\rangle_e$, which corresponds to a different subset of ions (frequency class) [41], the $|-\rangle_e$ level can be neglected.

In this archetypal SHB three-level structure, the continuous optical excitation (Fig. 2, left) is redistributed between the ground-state sublevels, in accordance with the branching ratio $\mathcal{R}$ from the excited state. SHB is a cumulative process that can fully polarize the spins, provided the spin relaxation is slow as compared to the optical pumping rate $\mathcal{R}/T_1^{\mathrm{opt}}$ where T_1^{opt} is the optical lifetime. Even if some population is left in the optically excited state, this latter decays in a characteristic time of T_1^{opt}, the spin lifetime appearing as a slower timescale on the population decay curve.

On the contrary, when spin relaxation is too fast, one cannot accumulate a spin population imbalance, and an

alternative measurement method to SHB is needed. Instead of using a continuous laser for optical pumping, we perform transient optical excitation as illustrated in Fig. 2 (right). The π pulse achieves transient spin imbalance between $|-\rangle_g$ and $|+\rangle_g$ by promoting the $|-\rangle_g$ population into the optical excited state. The rapid recovery, caused by spin cross-relaxation, can be probed on the optical $|-\rangle_g \rightarrow |-\rangle_e$ transition. Having no time to scan the probe frequency, as we did in SHB, we instead measure only the transmission of a weak and short probe pulse. Inversely, the spin lifetime appears as a rapid timescale on the population decay curve and T_1^{opt} as a longer tail.

These two complementary techniques, namely, accumulated SHB and optical inversion recovery (π-pulse excitation) as distinguished in Fig. 2, are used alternatively. In practice, if accumulated SHB is observed revealing a large FF lifetime, meaning significantly larger than $T_1^{\mathrm{opt}} = 11$ ms, the spin lifetime is extracted from the SHB decay. Otherwise, the optical inversion recovery is used. In short, as compared to T_1^{opt}, the FF lifetime would represent the long decay time of the population for SHB and the rapid one for optical inversion recovery.

As we will see in Sec. III B, for the 50-ppm $Er^{3+}:Y_2SiO_5$ sample, the optical inversion recovery is used exclusively because the spin lifetimes are short. For the 10-ppm sample, accumulated SHB and optical inversion recovery are used alternatively to cover the different orders of magnitude expected for the anisotropic coupling term (Sec. II).

B. Experimental results

The two crystals under study are monoclinic Y_2SiO_5, grown by Scientific Materials Corporation; erbium substitutes for yttrium at dopant concentrations of 10 and 50 ppm, respectively. Among the two crystallographic substitution sites, we consider the one at 1536.48 nm, referenced as site 1 [9]. We use a liquid helium cryostat to cool the crystal at 2 K and a superconducting coil, controlled by a low-voltage power supply, to generate a weak 0.15–0.3-mT magnetic field. We use the three optical extinction axis (D_1-D_2-b) as a reference frame. Light propagates along b, whereas the crystal is placed on a rotating mount (Attocube ANRv51/LT) so that the external magnetic field can be rotated in the whole D_1-D_2 plane.

As discussed in Sec. III A, to measure the spin lifetimes of the 10-ppm crystal, we implement the SHB experiment for angles from 60° to 180° where long lifetimes are observed. For angles ϕ from 5° to 55°, the spin lifetimes appear to be shorter than the optical lifetime so we use the optical inversion recovery technique. For the 50-ppm sample, the observed lifetimes are around or shorter than $T_1^{\mathrm{opt}} = 11$ ms for any angle. Therefore, the optical inversion recovery is implemented exclusively.

For both measurement techniques, the optical setup is the same. We split a Koheras narrow-band fiber laser in two beams, the pump and the probe. The pump is amplified with a ManLight erbium-doped fiber amplifier. These two beams are temporally shaped by acousto-optic modulators, controlled by an arbitrary wave-form generator (Tektronix AWG520). Then, pump and probe beams counterpropagate in the crystal with typical power of 20 mW and 100 μW, respectively. Finally,
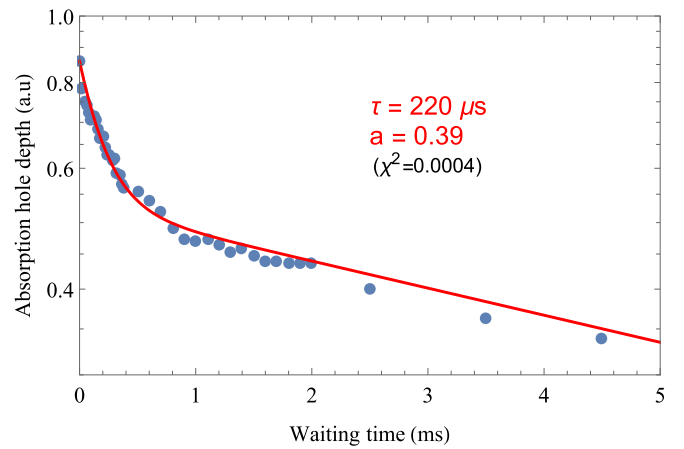

FIG. 3. Optical inversion recovery decay of the 10-ppm sample for **B** at 30°. We fit data with two exponential decay curves. One can extract the FF lifetime $\tau = 220 \, \mu$s from the shortest decay as discussed in the text. Its amplitude represents approximatively 40% of the whole population decay.

the probe is measured by an avalanche photodetector. The time sequences are different for the two techniques. For the SHB experiment, we use a 100-ms pump and 500-μs weak probe. We sweep the probe frequency to record the central hole area decays. For the optical inversion recovery, a 200-ns rms-duration pulse has a typical area of π (transient excitation, see Fig. 2). The mean transmission of a 10-μs probe pulse gives us the temporal evolution of the absorption at different waiting times after the π pulse (inversion recovery) The 10-μs probe duration gives the shortest measurable decay time that can be reached for concentrated samples. Figure 3 gives an example of the technique for the 10-ppm sample.

Both techniques exhibit decay curves characterizing the population dynamics. For the sake of simplicity, we assume that the decays are exponential following the conventional approach introduced in Sec. II. As discussed in Sec. III A in a simplified three-level system, these decays should have two characteristic times (see Fig. 3), T_1^{opt} and τ, where T_1^{opt} is the optical lifetime and τ the spin lifetime. We should be able to extract the spin lifetime by fitting data with the following formula:

$$\Delta_{\alpha L}(t) = \alpha L \left((1-a)e^{-\frac{t}{T_1^{\mathrm{opt}}}} + ae^{-\frac{t}{\tau}} \right), \qquad (14)$$

where T_1^{opt} is fixed to 11 ms. We choose to set the coefficients αL and a as free parameters even though they could be measured and calculated, respectively, by modeling the optical pumping dynamics. This is not the goal of the present paper, and we observe experimentally that their values depend on the efficiency of optical pumping or the π-pulse excitation, which varies significantly when rotating the sample.

However, in practice, Eq. (14) is not sufficient to fit the very different situations encountered when we change the angle of the magnetic field. Indeed, for a magnetic field of around 130°, the data from the SHB experiment reveal persistent holes already observed [24]. Their origin will be discussed in Sec. IV. Therefore, we have to include this effect, adding another exponential with a long decay time τ_{long} in the
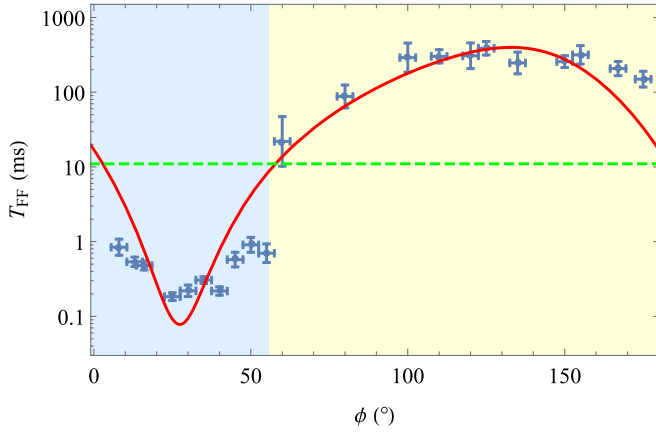
FIG. 4. Variation of the spin lifetime (log scale) with the angle ϕ of an external magnetic field of 0.3 mT in the $D_1 - D_2$ plane for the 10-ppm crystal. Blue shaded area, optical inversion recovery technique when the expected lifetime is typically shorter than $T_1^{\text{opt}} = 11$ ms (green dashed line). Yellow shaded area, accumulated SHB technique for longer lifetimes. The markers are the experimental measurements of τ, and the red curve is a fitting model that will be discussed in Sec. IV.

fit formula:

$$\Delta_{\alpha L}(t) = \alpha L\left((1 - a - b)e^{-\frac{t}{T_1^{\text{opt}}}} + ae^{-\frac{t}{\tau}} + be^{-\frac{t}{\tau_{\text{long}}}}\right). \quad (15)$$

To evaluate the FF rates, we extract the characteristic times τ. The long lifetime τ_{long} whose origin will be discussed in Sec. IV also exhibit an orientational dependency and varies by orders of magnitude from a few seconds to minutes, globally following the predicted FF anisotropy. As opposed to T_1^{opt}, which can be maintained as a fixed parameter for data fitting, τ_{long} should be kept as a free parameter (as the corresponding amplitude b) because it depends on the orientation.

The fitted value of τ for a varying magnetic field are represented in Figs. 4 and 5 for 10 and 50 ppm, respectively, and fitted with an elementary model that we will discuss in the following (Sec. IV).
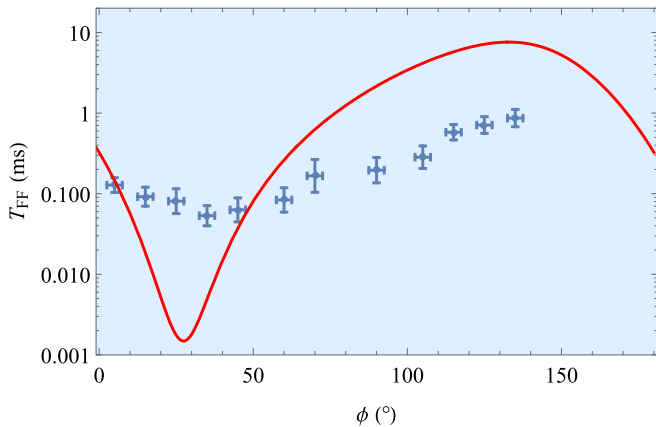

FIG. 5. Variation of the spin lifetime (log scale) with the angle ϕ of an external magnetic field of 0.15 mT in the $D_1 - D_2$ plane for the 50-ppm crystal. The experimental measurements correspond to the optical inversion recovery technique only.

IV. DISCUSSION

The strong anisotropy that can be inferred from Eq. (13), fully contained in $\Xi(\bar{\bar{g}}, \boldsymbol{B})$, is indeed observed in Fig. 4 for the 10-ppm sample. The anisotropy factor on the spin lifetime is 2.1×10^3 as the magnetic field is rotated in the $D_1 - D_2$ plane. This value can be compared to the expected 5.1×10^3 predicted from the $\Xi(\bar{\bar{g}}, \boldsymbol{B})$ dependency in Eq. (7). This argument apparently supports a conventional approach based on the FGR involving the average of the squared dipole-dipole coupling term. Unfortunately, the large anisotropy factor is not observed with the 50-ppm sample in Fig. 5: the observed ratio between the maximum and the minimum lifetimes is only 16 instead of the predicted 5.1×10^3.

The fitting parameter $\alpha_0 \Gamma_g$ can now be extracted separately for the two experimental sets of data, T_{FF} in Figs. 4 and 5 compared to $1/R_{FF}$, the decay time. Again, the angular dependency is fully contained in the anisotropic term $\Xi(\bar{\bar{g}}, \boldsymbol{B})$. We obtain for the fit $\alpha_0 \Gamma_g = \pi \times 1.8$ MHz for the 10-ppm sample (solid red line in Fig. 4) and $\alpha_0 \Gamma_g = \pi \times 0.9$ MHz for the 50-ppm sample (solid red line in Fig. 4). These values can be compared to the measured linewidth of the spin transition that can be obtained independently. Remember that α_0 is a dimensionless parameter scaling the minimum distance R_0. The spin inhomogeneous broadening can indeed be measured by the SHB technique. The area of the associated antihole (positioned at the ground-state splitting) corresponds to the inhomogeneous broadening of the spin levels [37]. The value varies with the magnetic field strength and orientation. We measure it for a 0.3-mT external field and with different orientations, and find values in the range $\pi \times [3.3, 9.6]$ MHz. Without going much deeper into detail, note that we here observe at 0.3 mT approximately the same spin linewidths (~ 5 MHz) as those measured via EPR at 60 mT [42]. Assuming a linear broadening with magnetic field, this difference corresponds to a factor of 15 in the broadening coefficients. This questions the origin of the inhomogeneous broadening, which may vary from low to high magnetic fields at different orientations. Even if we intentionally use a very weak magnetic field to reduce the spin inhomogeneous broadening and measure it conveniently with the SHB technique, further investigations are needed to fully understand the origin of the linewidth.

The values range is consistent with fitted values of $\alpha_0 \Gamma_g$ if α_0 is of the order of 1. The spatial range of validity of our approach R_0 is comparable with the average dopant spin distance. The parameter $\alpha_0 \Gamma_g$ is smaller for the 50-ppm sample. The spin inhomogeneous broadening is usually attributed to local lattice distortions [42], so there is no reason for Γ_g to vary with the concentration at this level. The apparent reduction of α_0 with the concentration and the difficulty to observe the predicted anisotropy of $\Xi(\bar{\bar{g}}, \boldsymbol{B})$ for the 50-ppm sample tell us that the dynamics is complex, thus requiring more sophisticated modeling than the elementary FGR-based estimation. It should nevertheless be noted that the overall dependency in density of interacting spins n_s, scaling as n_s^2 in Eq. (13) as discussed in Sec. II, predicts a factor of $5^2 = 25$ (between the 10- and 50-ppm samples) if the free scaling fitting parameter $\alpha_0 \Gamma_g$ was constant. This is not exactly the case, because $\alpha_0 \Gamma_g$ varies by a factor of 2, still smaller than 25.

So the FGR approach cannot be fully discarded and it seems valid to predict the correct orders of magnitude.

Before concluding, we expose our experimental sources of uncertainties that should be kept in mind for further modeling. To discuss the possible influences that are not included in our analysis, we can first mention the presence of Er^{3+} spins in the crystallographic site 2. They should not modify the FF rate of Er^{3+} ions in site 1 that we probe optically. Indeed, both sites have very different spin transitions (different g factors), so cross-relaxation between site 1 and 2 is off-resonant and therefore very unlikely. In other words, sites 1 and 2 should behave as two independent groups. This distinction is generally true, except if the sites have the same effective g factor. This singular situation occurs close to $\phi \sim 55°$ and $135°$ [10]. In that case, cross-relaxation between sites is resonant and may happen as soon as the spin transition difference (between sites) is smaller than Γ_g. This corresponds to a few degrees around $55°$ and $135°$ and may locally increase the FF rate, because the density of resonantly interacting ions is doubled. Around these two regions, few points of Fig. 4 seem to have a lower T_{ff} value that may confirm this extra interaction. This would deserve more investigations near $\phi \sim 135°$, for instance.

Another source of magnetic interaction is given by the so-called superhyperfine interaction [43] with the ligand (yttrium in that case) that we neglect in a first approach. The electronuclear spin coupling makes the electronic spin description significantly more complex, as recently discussed [44]. Despite the weakness of the interaction between Er^{3+} and the Y^{3+} nuclear spin, the Er^{3+}-Y^{3+} proximity makes the superhyperfine interaction comparable with the Er^{3+}-Er^{3+} electronic coupling in diluted samples (about 100 kHz in a 10-ppm crystal). Nevertheless, it should be kept in mind that these interactions, including the superhyperfine coupling, are weak compared to the spin inhomogeneous broadening Γ_g. So they should not drastically influence the FF dynamics, even if the exact coupling between Er^{3+}-Y^{3+} electronuclear mixed states still remains to be evaluated, first in a perturbative approach.

Finally, we want to discuss the presence of a long characteristic decay time named τ_{long} in Eq. (15). As described in Sec. III B, SHB experiments exhibit long-lived structures as observed earlier in similar conditions by Hastings-Simon *et al.* [24]. The coefficient b in Eq. (15) is around 0.1 for every orientation of the field. They could be attributed to the ^{167}Er isotope, which represents 22% of the ions and possesses a nuclear spin. They may exhibit slower FF rates because of their much weaker effective concentration, not only because of the 22% abundance, but also because their population is distributed among different hyperfine states making the resonant FF process much less likely. Additionally, the hyperfine coupling (electron-nuclear spin mixing) should significantly modify the cross-relaxation mechanism between sublevels, in other words, different interacting classes with different rates have to be defined to properly model the population dynamics, as recently considered for $Yb^{3+} : Y_2SiO_5$ [45]. A specific analysis with a 10- or 50-ppm isotopically pure ^{167}Er crystal would be interesting to explore the FF rate in the presence of hyperfine coupling. It should be noted that the situation has been recently explored with ^{145}Nd,

exhibiting similar timescales and a complex optical pumping dynamics [46].

V. CONCLUSION

We have shown experimentally that the erbium flip-flop dynamics is extremely anisotropic in Y_2SiO_5 for different orientations of the magnetic field. We have verified that an order-of-magnitude anisotropy in the g factor translates into 4 orders of magnitude for the flip-flop rate [17] in the most diluted sample. In this regime, typically at low magnetic field where many experiments are operated, this scaling severely limits the spin lifetime and may directly impact the optical pumping of ensembles. Depending on the sample under consideration, a proper choice of magnetic field orientation and dopant concentration has to be made.

It should be noted that the flip-flop reduction may impose a severe additional constraint on EPR experiments when, for example, a large microwave coupling is targeted. For example, in $Er^{3+} : Y_2SiO_5$, a bias magnetic field minimizing the flip-flops (large g factor) irremediably produces a weak coupling to the oscillating excitation field in the orthogonal direction. In other words, a proper trade-off has to be considered between cross-relaxation and a strong microwave coupling.

In any case, our study can be used as a guideline to understand the spin dynamics of other Kramers ions in different matrices.

APPENDIX: MATRIX ELEMENT ANALYTICAL FORMULA

We choose as local frame the one where the g tensor is diagonal (x, y, z). The effective magnetic field can be written as

$$\boldsymbol{B}_{\text{eff}} = \frac{1}{g_{\text{eff}}} \begin{pmatrix} g_x B_x \\ g_y B_y \\ g_z B_z \end{pmatrix} = B \begin{pmatrix} \sin \Theta \cos \Phi \\ \sin \Theta \sin \Phi \\ \cos \Theta \end{pmatrix}, \quad \text{(A1)}$$

where $B = ||\boldsymbol{B}||$, $g_{\text{eff}} = \sqrt{g_x^2 B_x^2 + g_y^2 B_y^2 + g_z^2 B_z^2}/B$, and (Φ, Θ) are the angular coordinates of $\boldsymbol{B}_{\text{eff}}$ in the (x, y, z) frame. Then we can write the 2×2 Zeeman Hamiltonian as

$$H_Z = -\mu_B g_{\text{eff}} B(\sin \Theta \cos \Phi S_x + \sin \Theta \sin \Phi S_y + \cos \Theta S_z).$$
$$\text{(A2)}$$

The eigenvalues of H_Z are $\pm \frac{1}{2} \mu_B g_{\text{eff}} B$ and the eigenstates are

$$|+\rangle = \cos \frac{\Theta}{2} |+1/2\rangle + \sin \frac{\Theta}{2} e^{i\Phi} |-1/2\rangle,$$

$$|-\rangle = \cos \frac{\Theta}{2} |-1/2\rangle - \sin \frac{\Theta}{2} e^{-i\Phi} |+1/2\rangle. \quad \text{(A3)}$$

We aim at calculating the dimensionless factor $\Xi(\bar{\bar{g}}, \boldsymbol{B})$ [see Eq. (7)]. Expressing the unit vector $\boldsymbol{u}_{ij}$ in terms of angular coordinates as

$$\boldsymbol{u}_{ij} = \frac{\boldsymbol{r}_{ij}}{r_{ij}} = \begin{pmatrix} \sin\theta\cos\phi \\ \sin\theta\sin\phi \\ \cos\theta \end{pmatrix}, \tag{A4}$$

we readily obtain

$$\begin{aligned}
\mathcal{A}(\phi,\theta) &= 3\langle - + |(\boldsymbol{\mu}_i \cdot \boldsymbol{r}_{ij})(\boldsymbol{\mu}_j \cdot \boldsymbol{r}_{ij})| + -\rangle/\mu_{\mathrm{B}}^2 \\
&= \tfrac{3}{4}[\sin^2\theta\cos^2\Theta\,\mathcal{R}^2 + g_z^2\cos^2\theta\sin^2\Theta \\
&\quad - 2g_z\sin\theta\cos\theta\sin\Theta\cos\Theta\,\mathcal{R} + \sin^2\theta\,\mathcal{I}^2],
\end{aligned} \tag{A5}$$

where $\Gamma = (g_x\cos\phi + ig_y\sin\phi)e^{-i\Phi} = \mathcal{R} + i\mathcal{I}$, and

$$\begin{aligned}
\mathcal{B} &= \langle - + |\boldsymbol{\mu}_i \cdot \boldsymbol{\mu}_j| + -\rangle\mu_{\mathrm{B}}^2 = \tfrac{1}{8}\big[2(g_x^2 + g_y^2) \\
&\quad - \sin^2\Theta(g_x^2 + g_y^2 - 2g_z^2) \\
&\quad - \sin^2\Theta\cos(2\Phi)(g_x^2 - g_y^2)\big].
\end{aligned} \tag{A6}$$

Since $\mathcal{A}(\phi,\theta)$ and $\mathcal{B}$ are real, the factor $\Xi(\bar{\bar{g}}, \boldsymbol{B})$ can be expressed as

$$\Xi(\bar{\bar{g}}, \boldsymbol{B}) = \langle[(\mathcal{A}(\phi,\theta) - \mathcal{B})]^2\rangle_{\theta,\phi}, \tag{A7}$$

where

$$\langle f(\theta,\phi)\rangle_{\theta,\phi} = \frac{1}{4\pi}\int_0^{2\pi} d\phi \int_0^{\pi} \sin\theta\, d\theta\, f(\theta,\phi). \tag{A8}$$

Noticing that $\langle\mathcal{A}(\phi,\theta)\rangle_{\phi,\theta} = \mathcal{B}$, we expand $\Xi(\bar{\bar{g}}, \boldsymbol{B})$ as

$$\begin{aligned}
\Xi(\bar{\bar{g}}, \boldsymbol{B}) &= \langle[\mathcal{A}(\phi,\theta)]^2\rangle_{\phi,\theta} + \mathcal{B}(\mathcal{B} - 2\langle\mathcal{A}(\phi,\theta)\rangle_{\phi,\theta}) \\
&= \langle[\mathcal{A}(\phi,\theta)]^2\rangle_{\phi,\theta} - \mathcal{B}^2. \tag{A9}
\end{aligned}$$

According to Eq. (A6), $\mathcal{B}$ can be expressed in terms of the three parameters

$$\begin{aligned}
S &= g_x^2 + g_y^2, \\
\Delta_1 &= g_x^2 + g_y^2 - 2g_z^2, \\
\Delta_2 &= g_x^2 - g_y^2,
\end{aligned} \tag{A10}$$

that characterize the anisotropy of the *g* tensor. The anisotropy between the longitudinal and transverse axis, and within the two transverse axis, is respectively represented by Δ_1 and Δ_2. In the case of an isotropic *g* tensor, $S = 2g_{\mathrm{eff}}^2$, and $\Delta_1 = \Delta_2 = 0$.

In the same way $\langle[\mathcal{A}(\phi,\theta)]^2\rangle_{\phi,\theta}$ can be expressed in terms of those anisotropy parameters:

$$\begin{aligned}
&\langle[\mathcal{A}(\phi,\theta)]^2\rangle_{\phi,\theta} \\
&= \frac{9}{80}\Big\{\big[\tfrac{2}{3}S - \tfrac{1}{2}\sin^2\Theta\,\Delta_1 + \tfrac{1}{2}\big(\cos^2\Theta - \tfrac{1}{3}\big)\cos(2\Phi)\Delta_2\big]^2 \\
&\quad + \tfrac{2}{9}\big[S - \cos(2\Phi)\Delta_2\big]^2 + \tfrac{1}{3}\cos^2\Theta\,\sin^2(2\Phi)\Delta_2^2\Big\}. \tag{A11}
\end{aligned}$$

[1] A. Abragam and B. Bleaney, *Electron Paramagnetic Resonance of Transition Ions* (Oxford University Press, Oxford, England, 2012).

[2] C. Grezes, B. Julsgaard, Y. Kubo, W. L. Ma, M. Stern, A. Bienfait, K. Nakamura, J. Isoya, S. Onoda, T. Ohshima, V. Jacques, D. Vion, D. Esteve, R. B. Liu, K. Mølmer, and P. Bertet, Phys. Rev. A **92**, 020301(R) (2015).

[3] S. Probst, H. Rotzinger, A. V. Ustinov, and P. A. Bushev, Phys. Rev. B **92**, 014421 (2015).

[4] L. A. Williamson, Y.-H. Chen, and J. J. Longdell, Phys. Rev. Lett. **113**, 203601 (2014).

[5] C. O'Brien, N. Lauk, S. Blum, G. Morigi, and M. Fleischhauer, Phys. Rev. Lett. **113**, 063603 (2014).

[6] X. Fernandez-Gonzalvo, Y.-H. Chen, C. Yin, S. Rogge, and J. J. Longdell, Phys. Rev. A **92**, 062313 (2015).

[7] A. M. Dibos, M. Raha, C. M. Phenicie, and J. D. Thompson, Phys. Rev. Lett. **120**, 243601 (2018).

[8] T. Zhong, J. M. Kindem, J. G. Bartholomew, J. Rochman, I. Craiciu, V. Verma, S. W. Nam, F. Marsili, M. D. Shaw, A. D. Beyer, and A. Faraon, Phys. Rev. Lett. **121**, 183603 (2018).

[9] T. Böttger, Y. Sun, C. W. Thiel, and R. L. Cone, Phys. Rev. B **74**, 075107 (2006).

[10] Y. Sun, T. Böttger, C. W. Thiel, and R. L. Cone, Phys. Rev. B **77**, 085124 (2008).

[11] D. M. B. P. Milori, I. J. Moraes, A. C. Hernandes, R. R. de Souza, M. S. Li, M. C. Terrile, and G. E. Barberis, Phys. Rev. B **51**, 3206 (1995).

[12] T. Böttger, C. W. Thiel, Y. Sun, and R. L. Cone, Phys. Rev. B **73**, 075101 (2006).

[13] R. Orbach, Proc. R. Soc. London, Ser. A **264**, 458 (1961).

[14] J. Van Vleck, Phys. Rev. **74**, 1168 (1948).

[15] A. Portis, Phys. Rev. **104**, 584 (1956).

[16] E. Saglamyurek, T. Lutz, L. Veissier, M. P. Hedges, C. W. Thiel, R. L. Cone, and W. Tittel, Phys. Rev. B **92**, 241111(R) (2015).

[17] E. Z. Cruzeiro, A. Tiranov, I. Usmani, C. Laplane, J. Lavoie, A. Ferrier, P. Goldner, N. Gisin, and M. Afzelius, Phys. Rev. B **95**, 205119 (2017).

[18] T. Böttger, C. W. Thiel, R. L. Cone, and Y. Sun, Phys. Rev. B **79**, 115104 (2009).

[19] M. Rančić, M. P. Hedges, R. L. Ahlefeldt, and M. J. Sellars, Nat. Phys. **14**, 50 (2018).

[20] T. Lutz, L. Veissier, C. W. Thiel, R. L. Cone, P. E. Barclay, and W. Tittel, Phys. Rev. A **94**, 013801 (2016).

[21] H.-S. Yang, S. Feofilov, D. K. Williams, J. C. Milora, B. M. Tissue, R. Meltzer, and W. Dennis, Phys. B: Condens. Matter **263**, 476 (1999).

[22] H.-S. Yang, K. Hong, S. Feofilov, B. M. Tissue, R. Meltzer, and W. Dennis, J. Lumin. **83**, 139 (1999).

[23] R. P. Budoyo, K. Kakuyanagi, H. Toida, Y. Matsuzaki, W. J. Munro, H. Yamaguchi, and S. Saito, Appl. Phys. Exp. **11**, 043002 (2018).

[24] S. R. Hastings-Simon, B. Lauritzen, M. U. Staudt, J. L. M. van Mechelen, C. Simon, H. de Riedmatten, M. Afzelius, and N. Gisin, Phys. Rev. B **78**, 085410 (2008).

[25] K. Heshami, D. G. England, P. C. Humphreys, P. J. Bustard, V. M. Acosta, J. Nunn, and B. J. Sussman, J. Mod. Opt. **63**, 2005 (2016).

[26] T. Asakura and I. Ando, *Solid State NMR of Polymers* (Elsevier, New York, 1998), Vol. 84.

[27] N. Bloembergen, Physica **15**, 386 (1949).

[28] N. Bloembergen, S. Shapiro, P. Pershan, and J. Artman, Phys. Rev. **114**, 445 (1959).

[29] E. Dikarov, O. Zgadzai, Y. Artzi, and A. Blank, Phys. Rev. Appl. **6**, 044001 (2016).

[30] S. Geschwind, *Electron Paramagnetic Resonance* (Plenum Publishing Corp., New York, 1972).

[31] R. C. Johnson, B. Z. Malkin, J. S. Lord, S. R. Giblin, A. Amato, C. Baines, A. Lascialfari, B. Barbara, and M. J. Graf, Phys. Rev. B **86**, 014427 (2012).

[32] L. Gomes, L. C. Courrol, L. V. G. Tarelho, and I. M. Ranieri, Phys. Rev. B **54**, 3825 (1996).

[33] C. Laplane, E. Zambrini Cruzeiro, F. Fröwis, P. Goldner, and M. Afzelius, Phys. Rev. Lett. **117**, 037203 (2016).

[34] F. de Seze, A. Louchet, V. Crozatier, I. Lorgeré, F. Bretenaker, J.-L. Le Gouët, O. Guillot-Noël, and P. Goldner, Phys. Rev. B **73**, 085112 (2006).

[35] S. R. Hastings-Simon, M. Afzelius, J. Minář, M. U. Staudt, B. Lauritzen, H. de Riedmatten, N. Gisin, A. Amari, A. Walther, S. Kröll, E. Cavalli, and M. Bettinelli, Phys. Rev. B **77**, 125111 (2008).

[36] M. Afzelius, M. U. Staudt, H. de Riedmatten, N. Gisin, O. Guillot-Noël, P. Goldner, R. Marino, P. Porcher, E. Cavalli, and M. Bettinelli, J. Lumin. **130**, 1566 (2010).

[37] B. Lauritzen, S. R. Hastings-Simon, H. de Riedmatten, M. Afzelius, and N. Gisin, Phys. Rev. A **78**, 043402 (2008).

[38] B. Lauritzen, N. Timoney, N. Gisin, M. Afzelius, H. de Riedmatten, Y. Sun, R. M. Macfarlane, and R. L. Cone, Phys. Rev. B **85**, 115111 (2012).

[39] S. Welinski, P. J. Woodburn, N. Lauk, R. L. Cone, C. Simon, P. Goldner, and C. W. Thiel, Phys. Rev. Lett. **122**, 247401 (2019).

[40] J. V. Rakonjac, Y.-H. Chen, S. P. Horvath, and J. J. Longdell, arXiv:1802.03862.

[41] M. Nilsson, L. Rippe, S. Kröll, R. Klieber, and D. Suter, Phys. Rev. B **70**, 214116 (2004).

[42] S. Welinski, C. Thiel, J. Dajczgewand, A. Ferrier, R. Cone, R. Macfarlane, T. Chanelière, A. Louchet-Chauvet, and P. Goldner, Opt. Mater. **63**, 69 (2017).

[43] O. Guillot-Noël, H. Vezin, P. Goldner, F. Beaudoux, J. Vincent, J. Lejay, and I. Lorgeré, Phys. Rev. B **76**, 180408(R) (2007).

[44] B. Car, L. Veissier, A. Louchet-Chauvet, J.-L. Le Gouët, and T. Chanelière, Phys. Rev. Lett. **120**, 197401 (2018).

[45] S. Welinski, Ph.D. thesis, Université de recherche Paris Sciences et Lettres Research University, 2018.

[46] E. Z. Cruzeiro, A. Tiranov, J. Lavoie, A. Ferrier, P. Goldner, N. Gisin, and M. Afzelius, New J. Phys. **20**, 053013 (2018).